



Preparation, characterization and visible-light-driven photocatalytic activity of Fe-doped titania nanorods and first-principles study for electronic structures

Jiaguo Yu^{*}, Quanjun Xiang, Minghua Zhou

State Key Laboratory of Advanced Technology for Material Synthesis and processing, Wuhan University of Technology, Luoshi Road 122#, Wuhan 430070, PR China

ARTICLE INFO

Article history:

Received 18 January 2009

Received in revised form 10 April 2009

Accepted 24 April 2009

Available online 3 May 2009

Keywords:

Fe-doped

Titanate nanotubes

Titania nanorods

Photocatalytic activity

Visible-light

DFT

ABSTRACT

Fe-doped TiO₂ (Fe-TiO₂) nanorods were prepared by an impregnating-calcination method using the hydrothermally prepared titanate nanotubes as precursors and Fe(NO₃)₃ as dopant. The as-prepared samples were characterized by scanning electron microscope, transmission electron microscope, X-ray diffraction, X-ray photoelectron spectroscopy, N₂ adsorption-desorption isotherms and UV-vis spectroscopy. The photocatalytic activity was evaluated by the photocatalytic oxidation of acetone in air under visible-light irradiation. The results show that Fe-doping greatly enhance the visible-light photocatalytic activity of mesoporous TiO₂ nanorods, and when the atomic ratio of Fe/Ti (R_{Fe}) is in the range of 0.1–1.0%, the photocatalytic activity of the samples is higher than that of Degussa P25 and pure TiO₂ nanorods. At R_{Fe} = 0.5%, the photocatalytic activity of Fe-TiO₂ nanorods exceeds that of Degussa P25 by a factor of more than two times. This is ascribed to the fact that the one-dimensional nanostructure can enhance the transfer and transport of charge carrier, the Fe-doping induces the shift of the absorption edge into the visible-light range with the narrowing of the band gap and reduces the recombination of photo-generated electrons and holes. Furthermore, the first-principle density functional theory (DFT) calculation further confirms the red shift of absorption edges and the narrowing of band gap of Fe-TiO₂ nanorods.

© 2009 Elsevier B.V. All rights reserved.

1. Introduction

In recent years, one-dimensional (1D) nanostructured materials have been extensively studied because of their distinctive geometries, novel physical and chemical properties and potential applications in nanoscale optical and electric devices [1–6]. Among the various oxide and non-oxide 1D nanostructured materials, titanate nanotubes have also received more and more attention due to their cheap fabrication, high specific surface area and pore volume and wide applications in photovoltaic cells, photocatalysis, catalytic supports and gas sensing since the innovative work was reported by Kasuga et al. [7–15]. Using a simple hydrothermal treatment of crystalline TiO₂ powders with NaOH aqueous solutions, high-quality titanate nanotubes with uniform diameters of around 10 nm were obtained and their specific surface area reached more than 400.0 m²/g [13,14]. Unfortunately, the prepared titanate nanotubes, nanobelts and nanowires by the hydrothermal method show almost no photocatalytic activity for the photocatalytic oxidation of acetone in our experiment [16–19]. Considering their large specific surface area, high pore volume and unique morphology, the obtained nanotubes will offer new

chance to design various 1D TiO₂-related photocatalytic materials by doping and calcinations [20–23].

To meet the increasingly stringent standards of environmental regulations, catalytic techniques are being applied in the fields of environmental protection. Photocatalysis is one technique that has great potential to control aqueous organic contaminants or air pollutants. It is believed to have several advantages over conventional oxidation processes, including (1) complete mineralization of the pollutants, (2) use of the near-UV or solar light, (3) no addition of other chemicals, and (4) operation at near room temperature [24–32]. Among various oxide semiconductor photocatalysts, titanium dioxide has been proved to be one of the best photocatalysts due to its biological and chemical inertness, strong oxidizing power, cost-effectiveness and long-term stability against photocorrosion and chemical corrosion for widespread environmental applications. However, due to its large band gap (3.2 eV), the currently used photocatalyst TiO₂ can only absorb a small fraction of solar energy, thus restricting its practical applications [33,34]. In view of the efficient utilization of solar energy, it is indispensable to develop a photocatalyst with high activities under visible-light irradiation [35,36]. Metal elements doping is one of the typical approaches to extend the spectral response of the titanium dioxide to visible-light region by providing defect states in the band gap [37–39]. Some metal elements such as Fe, Cr, Co, Mo and V have been employed to tune the electronic structure and

^{*} Corresponding author.

E-mail address: jiaguoyu@yahoo.com (J. Yu).

enhanced the photocatalytic activity of the titanium dioxide [33,40]. Among these elements, Fe has attracted special attention. For example, Choi et al. [40] reported the highest chloroform degradation efficiency under UV irradiation for a sample containing 0.5 (at.%) Fe^{3+} and the substitution of Ti^{4+} ions in the titania lattice by Fe^{3+} ions was favored. Zhu et al. [41] recently used a sol-gel method to prepare Fe-TiO_2 and studied the effect of Fe^{3+} doping concentration on the photoactivity of yellow XRG dye. Cong et al. [42] studied the co-doping effect of N and Fe on TiO_2 , which improved the activity under both visible and UV lights irradiation. It was commonly reported that the improvement of photocatalysts was attributed to the Fe^{3+} dopants which can help the separation of photo-generated electrons and holes, and also can absorb and utilize the visible light to photocatalyze the degradation of pollutants [43–45].

In this work, Fe-doped TiO_2 nanorods were prepared by a simple impregnating-calcination method using the hydrothermally prepared titanate nanotubes as precursors and $\text{Fe}(\text{NO}_3)_3$ as dopant. The photocatalytic activity of the samples was evaluated by the photocatalytic oxidation of acetone in air under visible-light irradiation. To the best of our knowledge, this is the first time to report the preparation and visible-light-driven photocatalytic activity of Fe-doped titania nanorods and first-principles study for their electronic structures.

2. Experimental details

2.1. Preparation of titanate nanotubes

Titanate nanotubes were prepared using a hydrothermal method similar to that described by Kasuga et al. [13,14]. TiO_2 used for the preparation of titanate nanotubes was Degussa P25 TiO_2 powders (P25) with crystalline structure of ca. 20% rutile and ca. 80% anatase and primary particle size of ca. 30 nm. In a typical synthesis, 1.5 g P25 was mixed with 140 ml of 10 M NaOH solution followed by hydrothermal treatment of the mixture at 150 °C in a 200 ml Teflon-lined autoclave for 48 h. After hydrothermal reaction, the precipitate was separated by filtration and washed with a 0.1 M HCl solution and distilled water until the pH value of the rinsing solution reached ca. 6.5, approaching the pH value of the distilled water. The washed samples were dried in a vacuum oven at 80 °C for 8 h.

2.2. Preparation of Fe-doped TiO_2 nanorods

Fe-doped TiO_2 (Fe-TiO_2) nanorods were prepared by an impregnating-calcination method using the as-prepared titanate nanotubes as precursors. The detailed experimental procedures are as follows: 0.2 g of titanate nanotube powders was mixed with 25 ml of ferric nitrate ($\text{Fe}(\text{NO}_3)_3$) aqueous solution. In order to eliminate the effect of pH, the pH values of all mixed solutions were adjusted to 5 with a dilute nitrate acid solution (0.1 M). The suspensions were stirred for 0.5 h and then placed at room temperature for 48 h. After that, the mixed solution was dried in an oven at 100 °C for 5 h to evaporate the water. The dried samples were ground and finally calcined at 500 °C in air for 1.5 h. The nominal atomic ratios of Fe to Ti, which hereafter was designated as R_{Fe} , were 0, 0.1, 0.25, 0.5 and 1.0 atomic% (at.%), and the obtained powders were labeled as R0, R0.1, R0.25, R0.5 and R1.0, respectively. The color of the calcined powder samples slightly changed and was from white to slight red with increasing R_{Fe} .

2.3. Characterization

The morphology observation was performed on a S-4800 field emission scanning electron microscope (SEM, Hitachi, Japan).

Transmission electron microscopy (TEM) and high-resolution transmission electron microscopy (HRTEM) analyses were conducted with a JEM-2100F electron microscope (JEOL, Japan), using a 200 kV accelerating voltage. X-ray diffraction (XRD) patterns, obtained on a D/MAX-RB X-ray diffractometer (Rigaku, Japan) using $\text{Cu K}\alpha$ radiation at a scan rate (2θ) of $0.05^\circ \text{ s}^{-1}$, were used to determine the identity of any phase present and their crystallite size. The accelerating voltage and the applied current were 40 kV and 80 mA, respectively. X-ray photoelectron spectroscopy (XPS) measurements were performed on a VG ESCALAB 210 XPS system with $\text{Mg K}\alpha$ (1253.6 eV) source. All the binding energies were referenced to the C 1s peak at 284.8 eV of the surface adventitious carbon. The Brunauer–Emmett–Teller (BET) surface areas (S_{BET}) of the samples were analyzed by nitrogen adsorption on an ASAP 2020 nitrogen adsorption apparatus (Micromeritics Instruments, USA). All the samples were degassed at 180 °C prior to nitrogen adsorption measurements. The BET surface area was determined by a multi-point BET method using the adsorption data in the relative pressure (P/P_0) range of 0.05–0.3. The desorption isotherm was used to determine the pore size distribution using the Barret–Joyner–Halender (BJH) method assuming cylindrical pore [46–48]. The nitrogen adsorption volume at the relative pressure (P/P_0) of 0.994 was used to determine the pore volume and average pore size. UV–vis spectra were obtained on an UV–vis spectrophotometer (UV-2550, Shimadzu, Japan). BaSO_4 was used as a reflectance standard in the UV–vis diffuse reflectance experiment.

2.4. Analysis of hydroxyl radicals ($\cdot\text{OH}$)

The formation of hydroxyl radicals ($\cdot\text{OH}$) on the surface of photo-illuminated TiO_2 was detected by the photoluminescence (PL) technique using terephthalic acid as a probe molecule, which readily reacts with $\cdot\text{OH}$ to produce highly fluorescent product, 2-hydroxyterephthalic acid. The method relies on the PL signal at 425 nm of 2-hydroxyterephthalic acid. The PL intensity of 2-hydroxyterephthalic acid is proportional to the amount of $\cdot\text{OH}$ produced on the surface of TiO_2 [49,50]. Experimental procedures were as follows; 0.1 g of TiO_2 powder sample was dispersed in a 20 ml of the 5×10^{-4} M terephthalic acid aqueous solution with a concentration of 2×10^{-3} M NaOH in a dish with a diameter of about 9.0 cm at ambient temperature. A 15 W daylight lamp (6 cm above the dishes) was used as a light source. The integrated visible-light intensity measured with a visible-light radiometer (Model: FZ-A, made in Photoelectric Instrument Factory of Beijing Normal University) was $2.9 \pm 0.1 \text{ mW/cm}^2$ with the wavelength range of 400–1000 nm. PL spectra of generated 2-hydroxyterephthalic acid were measured on a Hitachi F-7000 fluorescence spectrophotometer. After visible-light irradiation for every 15 min, the reaction solution was filtrated to measure the increase in the PL intensity at 425 nm of 2-hydroxyterephthalic acid excited by 315 nm light.

2.5. Measurement of photocatalytic activity

The visible-light photocatalytic activity experiments on the prepared samples and P25 for the photocatalytic oxidation of acetone in air were performed at ambient temperature using a 15 L rectangular photocatalytic reactor, as previously reported [51,52]. The photocatalysts were prepared by coating an aqueous suspension of the samples onto three dishes with diameters of 9.0 cm. The weight of catalysts used for each experiment was kept at ca. 0.3 g. The dishes containing catalysts were dried in an oven at 100 °C for about 2 h to evaporate the water and then cooled to room temperature before used. After sample-coated dishes were placed in the reactor, a small amount of acetone was injected into the reactor with a micro-syringe. The acetone vapor was allowed to reach adsorption equilibrium with catalysts in the reactor in the

dark prior to visible-light irradiation. The analysis of acetone, carbon dioxide and water vapor concentration in the reactor was conducted online with a Photoacoustic Field Gas-Monitor (INNOVA Air Tech Instruments Model 1412). The initial concentration of acetone after adsorption equilibrium was controlled to 400 ± 10 ppm for all experiments, which remained constant for about 10 min until a 15 W daylight lamp (6 cm above the dishes) in the reactor was switched on. A UV cutoff filter (1 cm below the lamp) was used to remove any radiation below 400 nm and to ensure illumination by visible-light only. The integrated visible-light intensity was measured with a FZ-A visible-light radiometer was 2.9 ± 0.1 mW/cm². The initial concentration of water vapor was 1.20 ± 0.01 vol%, and the initial temperature was 25 ± 1 °C. Each set of experiment was performed for 90 min. The photocatalytic activity of the samples can be quantitatively evaluated by comparing the decrease of acetone concentration and increase of produced CO₂ concentration within 90 min.

3. Computational details

All calculations were performed using the density functional theory (DFT) based on CASTEP software package within the generalized gradient approximation (GGA), and the interaction between the valence electrons and ionic core was described by the Perdew-Wang 91 gradient-corrected functional [53]. We simulated Fe doping effects using $2 \times 2 \times 1$ (48-atom) anatase supercell and replaced Ti atoms by one and two Fe atoms corresponding to

concentration ratios of $x = 1/16$ and $1/8$ in (Fe_xTi_{1-x})O₂. The calculated crystal parameters of the unit bulk anatase TiO₂ are $a = 3.785$ Å and $c = 9.514$ Å, which are consistent with the experimental data. The Monkhorst-Pack [54] grid with $5 \times 5 \times 2$ k points was used for integration in the Brillouin zone of the supercell, and the plane-wave kinetic energy cutoff was set to 340 eV. The mechanical equilibrium was achieved through conjugate gradient minimization of the total energy to a tolerance of 2×10^{-5} eV, the forces to a tolerance of 0.05 eV Å⁻¹, and the atomic positions to a tolerance of 2×10^{-3} Å.

4. Results and discussions

4.1. Morphology and structure of titanate nanotubes and Fe-TiO₂ nanorods

Fig. 1a shows TEM images of titanate nanotubes prepared by the hydrothermal method (see Section 2). A large amount of nanotubes with diameters of about 7–15 nm and lengths of several hundred nanometers could be easily obtained. HRTEM images (inset in a) indicate that the prepared nanotubes possess uniform inner and outer diameters along their length and the nanotubes are multi-wall and open-ended. Fig. 1b shows the SEM images of Fe-TiO₂ nanorods prepared at $R_{\text{Fe}} = 0.5$ and calcined at 500 °C. The prepared nanorods have diameters of about 8–15 nm and a length of several hundreds of nm. TEM image (Fig. 1c) further confirms that the calcined titanate nanotubes turn into the nanorods, in agreement

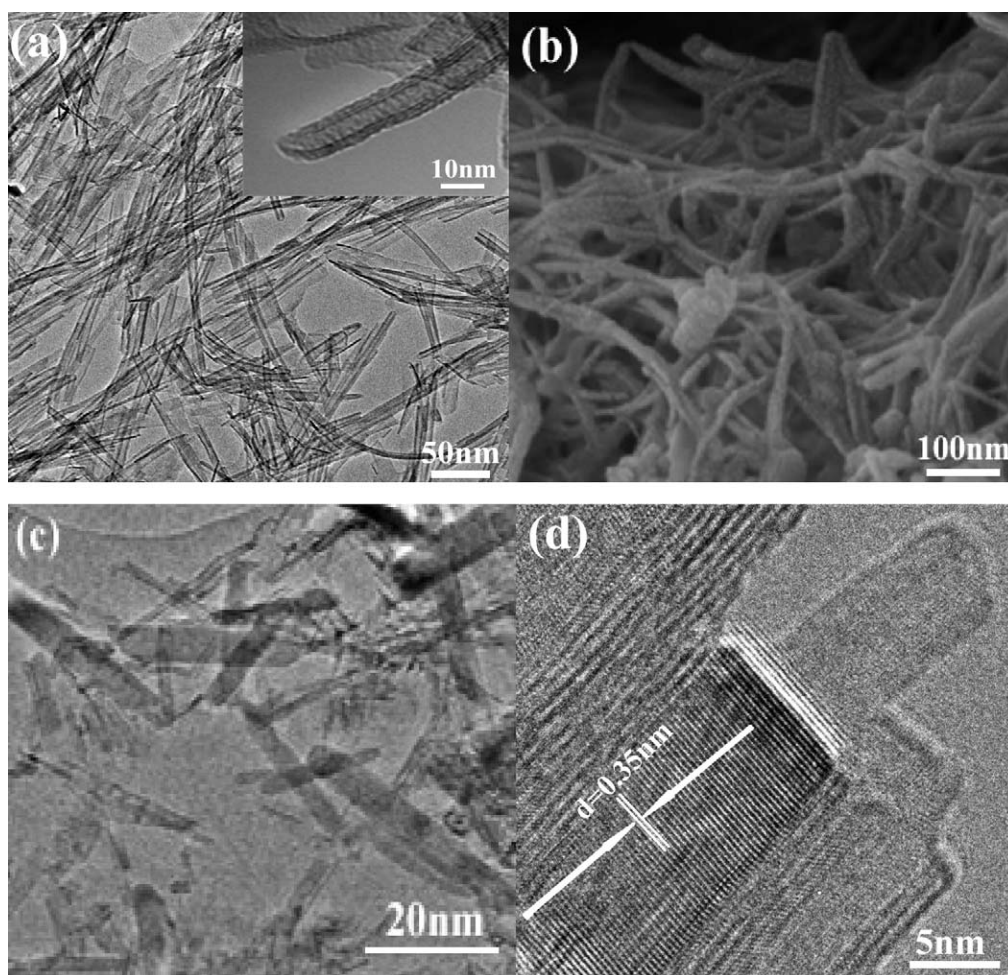


Fig. 1. TEM (a) and HRTEM images (inset in a) of the hydrothermally prepared titanate nanotubes; and SEM (b), TEM (c) and HRTEM images (d) of Fe-TiO₂ nanorods prepared at $R_{\text{Fe}} = 0.5$ and calcined at 500 °C.

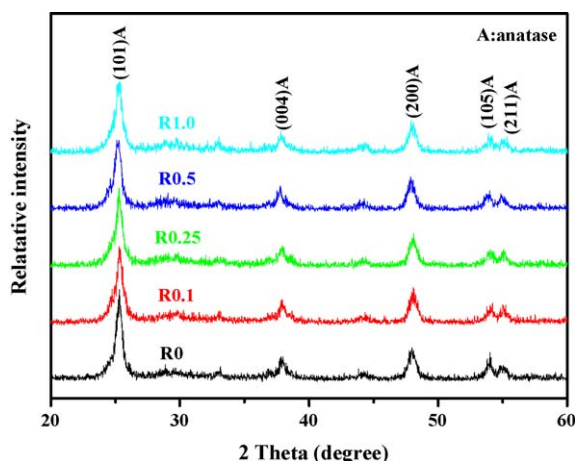


Fig. 2. XRD patterns of the Fe-TiO₂ nanorods prepared at different R_{Fe} .

with the previous results [9,55]. HRTEM images (Fig. 1d) suggest that the obtained TiO₂ nanorods are mainly a single crystalline structure in anatase phase. The inter-planar spacing of the nanorods is calculated to be ca. 0.35 nm, corresponding to the (1 0 1) crystal plane of anatase.

4.2. XRD study

XRD was used to identify and determine the phase structure, crystallite size and relative crystallinity of the samples. Fig. 2 shows XRD patterns of pure TiO₂ and Fe-TiO₂ nanorods prepared at different R_{Fe} . The diffraction peaks of all samples are ascribed to the diffraction peaks of TiO₂ anatase phase [JCPDS No. 21-1272, space group: $I4_1/amd$ (1 4 1)]. Further observation shows that with increasing R_{Fe} , XRD peak intensities of anatase steadily become weaker and the width of XRD diffraction peaks of anatase becomes slightly wider, indicating the formation of smaller TiO₂ crystallites and decrease of crystallinity (as shown in Table 1). The crystallinity of anatase phase is quantitatively evaluated via the relative intensity of the (1 0 1) diffraction peak of the anatase [51]. The Fe₂O₃ or Fe_xTi_yO_z phases are not found in the XRD patterns. This is ascribed to the fact that the concentration of Fe-doping is so low that it cannot be detected by XRD. On the other hand, the radius of Ti⁴⁺ (0.68 Å) and Fe³⁺ (0.64 Å) is almost same, therefore, the Fe³⁺ ions can enter into the crystal structure of titania and locate at interstices or occupy some of the lattice sites of TiO₂, forming an iron–titanium solid solution [56]. This is also further confirmed by the XPS results.

4.3. XPS study

In order to analyze chemical composition of the prepared Fe-TiO₂ nanorods and to identify the chemical status of Fe element in the samples, the samples were characterized by XPS. Fig. 3 presents the XPS survey spectrum of the Fe-TiO₂ nanorods

prepared at $R_{Fe} = 0.5$. The Fe-TiO₂ nanorods contain Ti, O, C and Fe elements, with sharp photoelectron peaks appearing at binding energies of 458 (Ti 2p), 531 (O 1s) and 285 eV (C 1s) and a weak photoelectron peak at 711 eV (Fe 2p). The carbon peak is attributed to adventitious hydrocarbon from XPS instrument itself. The high-resolution XPS spectrum (inset in Fig. 3) of the Fe 2p_{3/2} region of corresponding sample indicates that the peak at 710.5 eV is symmetrical and can be ascribed to Fe³⁺ ions. This is not difficult to be understood because dopant is Fe(NO₃)₃. Thus, the Fe element in the samples exists mainly in the +3 oxidation state (Fe³⁺). Since the radius of Fe³⁺ and Ti⁴⁺ is similar, the Fe³⁺ could be incorporated into the lattice of TiO₂ to form Ti–O–Fe bonds in the Fe-TiO₂ nanorods by calcination at 500 °C in air [55–57]. This is further confirmed by the chemical binding energy at 710.5 eV of Fe³⁺, which is different from that of Fe³⁺ in Fe₂O₃ (at 710.9 eV) [58]. Variations in the elemental binding energies (the chemical shifts) (0.4 eV) arise from the difference in the chemical potential and polarizability of Fe-TiO₂ nanorods and Fe₂O₃ [58]. The exact amount of surface Fe elements in Fe-TiO₂ nanorods ($R_{Fe} = 0.5$) is further characterized by XPS and their surface atomic percentage is 1.82%. This atomic percentage is not in agreement with the initial nominal atomic ratio of the sample. The higher surface iron concentration indicates that during the impregnating-calcination, a certain amount of iron is accumulated in the surface layer probably due to the transfer of iron from the inner to the surface of the Fe-TiO₂ nanorods [59].

4.4. BET surface areas and pore distributions

Fig. 4 shows nitrogen adsorption–desorption isotherms and corresponding pore size distribution curves (inset) of the Fe-TiO₂ nanorods. The other Fe-doped and un-doped samples have similar isotherms and pore size distribution (not shown here). The Fe-TiO₂ nanorod powders have isotherms of type IV and hysteresis loops of type H3 at relative pressure range of 0.8–1.0, indicating the presence of mesopores (2–50 nm). Moreover, the observed hysteresis loop approaches $P/P_0 = 1$, suggesting the presence of macropores (>50 nm). The pore size distributions (inset) indicate a wide distribution range from 10 to over 100 nm. The pore volumes of the pure and Fe-TiO₂ nanorods prepared at $R_{Fe} = 0.5$ are 0.18 and 0.23 cm³/g, respectively (see Table 1). In fact, the nanorods do not contain mesopores and macropores. Therefore, the existing nanopores (or pore volume) are from the aggregation of nanorods. Such organized porous structures are extremely useful in photocatalysis as they will provide efficient transport pathways to reactant molecules and products. Table 1 also shows that with increasing R_{Fe} , specific surface areas and pore volume increase, however, average pore size slightly decreases due to the suppression of crystallite growth.

4.5. UV–vis diffuse reflectance spectra

UV–vis diffuse reflectance spectra of the pure and Fe-TiO₂ nanorods are shown in Fig. 5. The onset of the absorption edge for pure TiO₂ nanorods is at ca. 390 nm, which is consistent with the

Table 1
Effects of R_{Fe} on physical properties of Fe-TiO₂ nanorods calcined at 500 °C.

Samples	Phase ^a	Crystalline size (nm) ^b	Surface area (m ² /g)	Pore volume (cm ³ /g)	Average pore size (nm)
R0	A	14.9 (1.00)	65.1	0.18	18.1
R0.1	A	13.4 (0.90)	73.9	0.19	16.7
R0.25	A	13.1 (0.88)	79.2	0.19	15.3
R0.5	A	12.0 (0.81)	82.3	0.23	14.4
R1.0	A	11.4 (0.77)	85.6	0.24	13.1

^a A denote anatase.

^b Average crystalline size of TiO₂ was determined by XRD using Scherrer equation. Relative anatase crystallinity: the relative intensity of the diffraction peak from the anatase (1 0 1) plane (indicated in parentheses, reference sample: R0).

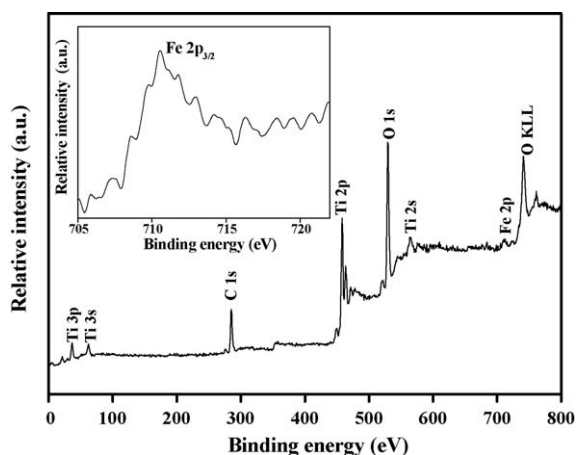


Fig. 3. XPS survey spectrum of the Fe-TiO₂ nanorods prepared at $R_{Fe} = 0.5$ and high resolution XPS spectrum (inset) of the Fe 2p_{3/2} region for corresponding sample.

intrinsic bandgap absorption of pure anatase TiO₂ (~ 3.2 eV). It is apparent that the diffuse reflectance spectra of all Fe-TiO₂ nanorods exhibit a red shift and increased absorption in the visible-light range. With increasing R_{Fe} , the absorption increases. The absorptions in the visible region may be induced by a sub-band-gap transition corresponding to the excitation of 3d electrons of Fe³⁺ to TiO₂ conduction band (charge transfer transition) at 415 nm and the d–d transition ${}^2T_{2g} \rightarrow {}^2A_{2g}$, ${}^2T_{1g}$ of Fe³⁺ or the charge transfer transition between iron ions ($Fe^{3+} + Fe^{3+} \rightarrow Fe^{4+} + Fe^{2+}$) at 500 nm, leading to a decrease in the energy band gap [41,60]. Undoubtedly, these results reveal that the iron ions are indeed incorporated into the lattice of TiO₂, thus altering its crystal and electronic structures.

The absorption edges shift toward longer wavelengths for the as-prepared Fe-TiO₂ nanorod powders. The inset in Fig. 5 clearly shows the incorporation of iron make the band gap energy smaller. Band gap energy can be estimated from a plot of $(\alpha h\nu)^2$ versus photon energy ($h\nu$). The intercept of the tangent to the plot will give a good approximation of the band gap energy for TiO₂ [61]. The absorption coefficient α could be calculated according to the Kubelka–Munk method based on the diffuse reflectance spectra [61–63]. The band gap energies estimated from the intercept of the tangents of the plots are 3.19, 3.14, 3.10, 3.04 and 2.97 eV for different doping concentration at 0, 0.1, 0.25, 0.5 and 1.0 (at%), respectively. The band gap energies decrease with increasing Fe-doping concentration. The reason may be that the doping iron ions can form a dopant level near the valence band of TiO₂ and reduce

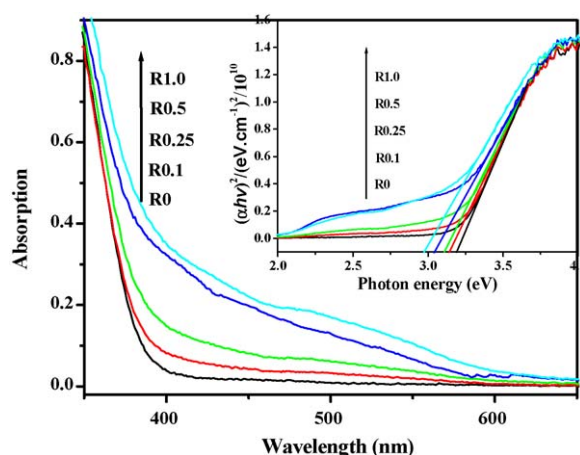


Fig. 5. UV–vis diffuse reflectance spectra of the pure and Fe-TiO₂ nanorods prepared at different R_{Fe} . The inset shows the plots of $(\alpha h\nu)^2$ versus $h\nu$ for band gap energies.

the band gap of TiO₂ [34]. The electronic transition from the modified dopant band to the conduction band can effectively improve the photocatalytic activity in visible-light region.

4.6. Hydroxyl radical analysis

Fig. 6a shows the changes of PL spectra of terephthalic acid solution with irradiation time. A gradual increase in PL intensity at about 425 nm is observed with increasing irradiation time.

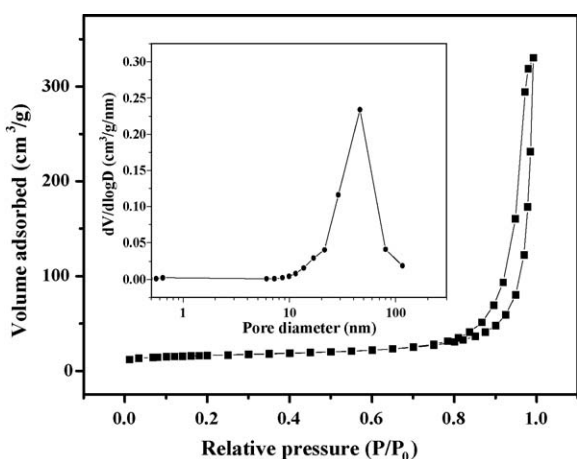


Fig. 4. Nitrogen adsorption–desorption isotherms and corresponding pore size distribution curves (inset) of the Fe-TiO₂ nanorods prepared at $R_{Fe} = 0.5$.

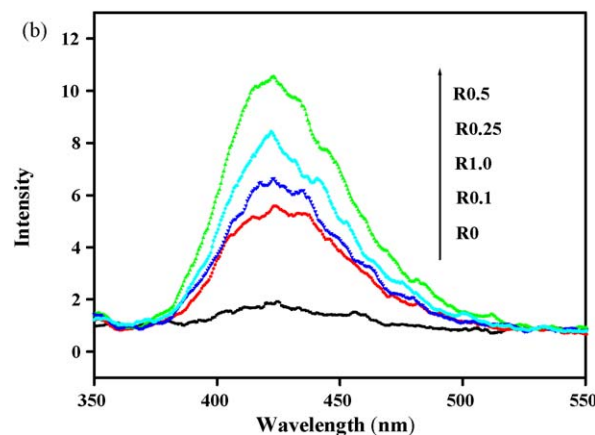
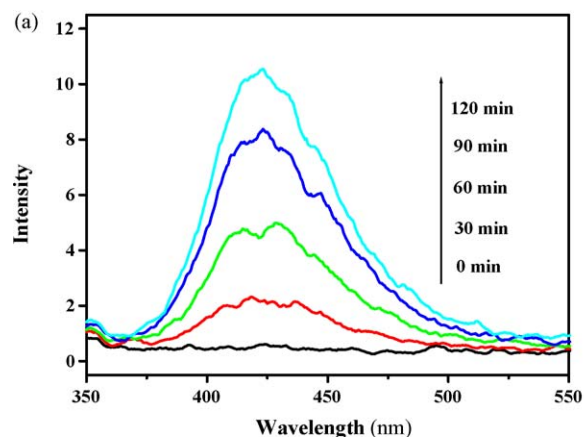


Fig. 6. (a) PL spectral changes with irradiation time on the R0.5 sample in a 5×10^{-4} M basic solution of terephthalic acid and (b) the dependence of the PL intensity on R_{Fe} at a fixed 120 min.

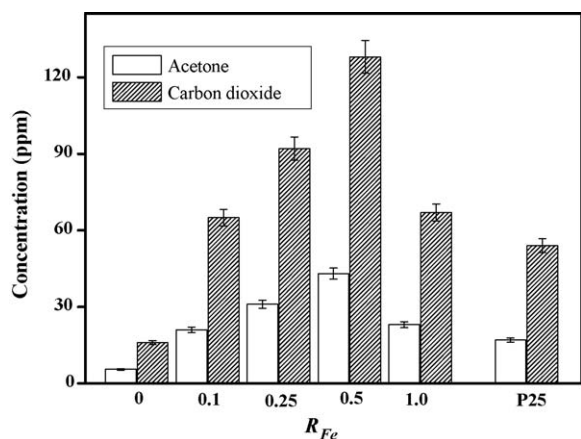


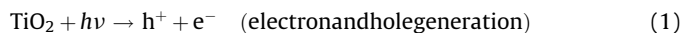
Fig. 7. Comparison of photocatalytic activity of the pure and Fe-TiO₂ nanorods prepared at different R_{Fe} and P25 for photocatalytic oxidation of acetone: The dependence of the decrease of acetone concentration and increase of produced CO₂ concentration (ppm) on R_{Fe} within 90 min.

However, no PL increase is observed in the absence of visible light or TiO₂ samples. This suggests that the fluorescence is from the chemical reactions between terephthalic acid and ·OH formed at the TiO₂/water interface via photocatalytic reactions [49,50]. Fig. 6b shows the dependence of PL intensity on R_{Fe} . Usually, PL intensity is proportional to the amount of produced hydroxyl radicals. It can be easily seen that at a fixed time (120 min), the formation rate of OH radicals on the Fe-TiO₂ nanorods is larger than that of the pure TiO₂ nanorods. This implies that the Fe-TiO₂ nanorods have higher visible-light photocatalytic activity than pure TiO₂ nanorods. Further observation (from Figs. 6b and 7) shows that PL intensity has a positive relation with photocatalytic activity. Especially, at $R_{Fe} = 0.5$, the sample has strongest PL intensity, implying a highest photocatalytic activity.

4.7. Photocatalytic activity

The photocatalytic activity of the pure and Fe-TiO₂ nanorods was evaluated by photocatalytic oxidation of acetone in air under visible-light irradiation. Fig. 7 shows the dependence of the decrease of acetone concentration and increase of produced CO₂ concentration (ppm) on R_{Fe} . For comparison, the photocatalytic activity of P25 was also tested under identical experimental conditions. As is known, P25 also shows visible-light photocatalytic activity (see Fig. 7) because P25 contains about 20–25% rutile, which has a band gap of 3.0 eV (~413 nm) resulting in visible-light absorption. R_{Fe} exhibits a great effect on the photocatalytic activity of Fe-TiO₂ nanorods. With increasing R_{Fe} , the photocatalytic activity of the sample increases rapidly and reaches a maximum

value at $R_{Fe} = 0.5$, and its activity exceeds that of P25 by more than two times. Then, the activity obviously decreases with further increasing R_{Fe} . This is due to the fact that a small amount of Fe³⁺ can act as a temporary photo-generated electron or hole-trapping site and inhibits the recombination of photo-generated charge carriers and prolongs their lifetime [9], which can be schematically shown in Fig. 8. The detailed reaction steps are as follows:



From the viewpoint of crystal field theory, Fe⁴⁺ and Fe²⁺ are relatively unstable as compared to Fe³⁺, which have half-filled d orbital (d⁵), as shown in Fig. 9. This kind of electron configuration has a special stability. Therefore, there is a tendency for the transfer of the trapped charge carriers from Fe²⁺ or Fe⁴⁺ to the adsorbed O₂ and surface hydroxyl (–OH), respectively, to regenerate Fe³⁺. These new produced active species (such as ·OH and O₂[–]) will initiate the following photocatalytic reactions [40]. It should be noted that the photocatalytic activity of Fe-TiO₂ nanorods is strongly dependent on the dopant concentration since the Fe³⁺ ions can serve not only as a mediator of interfacial charge transfer but also as a recombination center. In this study, an optimal dopant concentration is 0.5 at.%. Above that concentration, Fe³⁺ ions steadily become recombination centers and the activity steadily decreases because Fe³⁺ ions gradually act as recombination centres through quantum tunneling [40,55,64]. Therefore, it is not difficult to understand that the Fe-TiO₂ nanorods have higher photocatalytic activity than P25. Moreover, Fe-TiO₂ nanorods have one-dimensional nanostructure, larger specific surface areas and pore volume, a stronger absorption in the UV–vis range and red shift of absorption edges. These factors will also enhance the visible-light photocatalytic activity of Fe-TiO₂ nanorods.

4.8. Theoretical calculations

Our DFT calculations show the band gap of about 2.46 eV (see Fig. 10A) at Γ point for un-doped TiO₂, which is smaller than the experimental value 3.20 eV. This underestimation of the band gap is due mainly to the well-known shortcoming of exchange-correlation functional in describing excited states [65]. For the Fe-TiO₂ nanorods, the band gaps are calculated to be about 2.26 (Fig. 10B) and 2.12 eV (Fig. 10C) for concentrations ratios of $x = 1/16$ and $1/8$ in

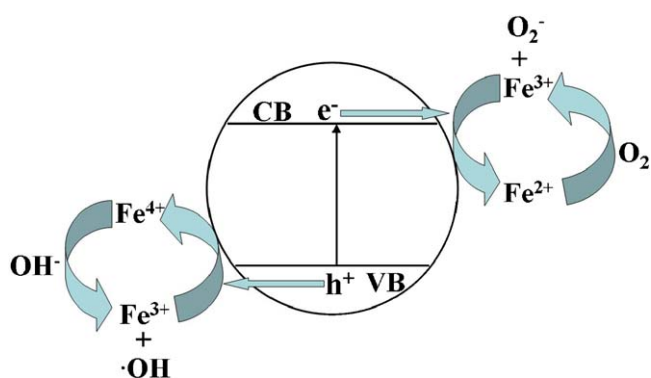


Fig. 8. Schematic diagram for Fe³⁺ acting as a mediator of interfacial charge transfer.

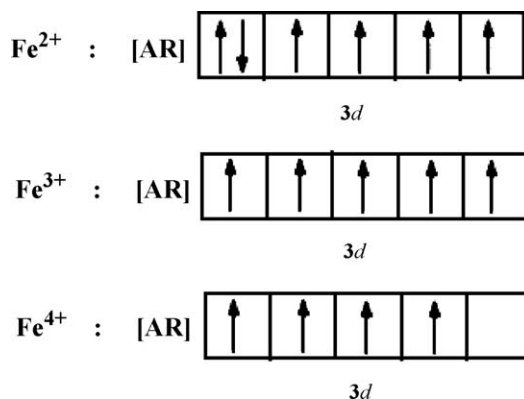


Fig. 9. The electron configuration of Fe²⁺, Fe³⁺ and Fe⁴⁺.

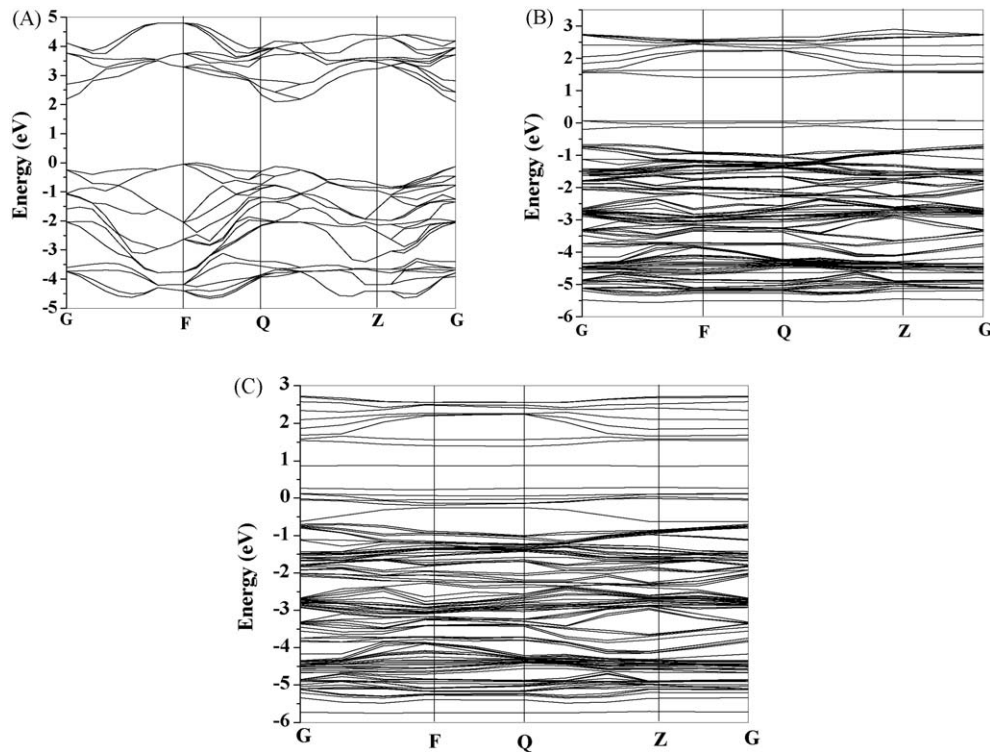


Fig. 10. Band structure plots for (A) TiO_2 , (B) $(\text{Fe}_{1/16}\text{Ti}_{15/16})\text{O}_2$ and (C) $(\text{Fe}_{1/8}\text{Ti}_{7/8})\text{O}_2$.

$(\text{Fe}_x\text{Ti}_{1-x})\text{O}_2$, respectively. Since the experimental band gap of undoped TiO_2 is obtained by adding 0.74 eV to the calculated band gap, it is practical to correct the underestimation of the band gaps of Fe-TiO_2 by adding 0.74 eV to the calculated band gap (scissor operation). Thus, the corrected band gaps for the concentrations ratios of $x = 1/16$ and $1/8$ in $(\text{Fe}_x\text{Ti}_{1-x})\text{O}_2$ are 3.00 and 2.86 eV, respectively. Hence, the band gap of Fe-TiO_2 nanorods decreases dramatically, indicating that the excitation requires less energy and

the absorption edges have a distinct red shift with respect to that of pure TiO_2 , which agrees well with our UV–vis absorption experimental results.

To examine the origin of the electronic structure modification of Fe-TiO_2 , the total density of states (TDOS) and projected density of states (PDOS) of $(\text{Fe}_{1/16}\text{Ti}_{15/16})\text{O}_2$ and $(\text{Fe}_{1/8}\text{Ti}_{7/8})\text{O}_2$ are plotted in Fig. 11A and B, respectively. For comparison, the TDOS and PDOS of the pure anatase are also plotted. From Fig. 11A(a) and B(a), we can

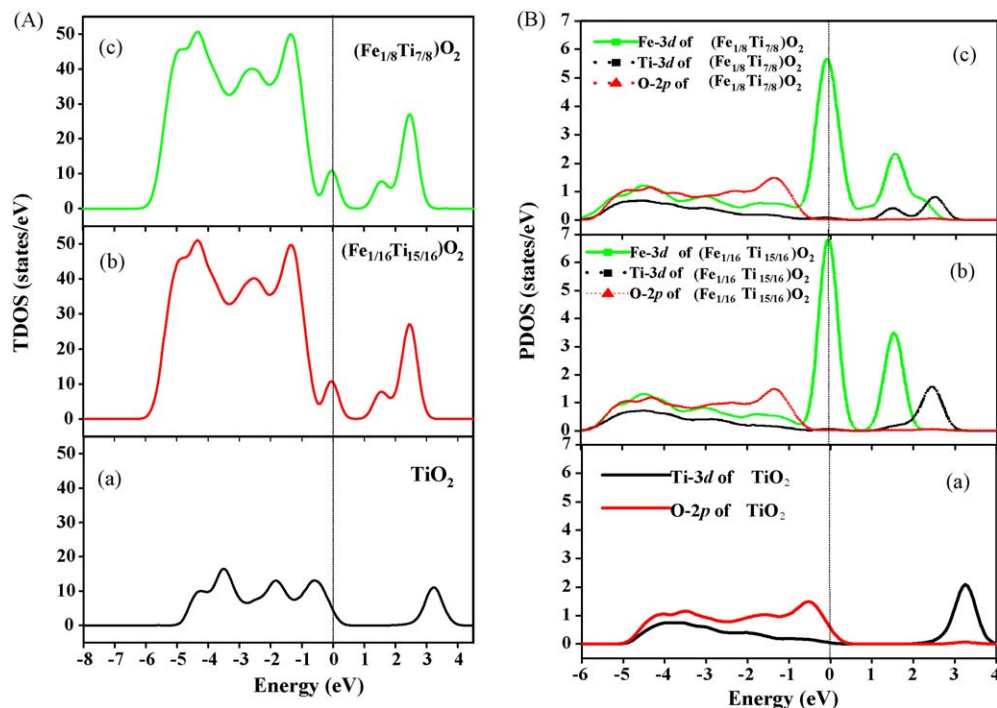


Fig. 11. (A) Total density of states (TDOS) and (B) projected density of states (PDOS) for 48-atom anatase supercell: (a) TiO_2 , (b) $(\text{Fe}_{1/16}\text{Ti}_{15/16})\text{O}_2$ and (c) $(\text{Fe}_{1/8}\text{Ti}_{7/8})\text{O}_2$.

see that O 2p states dominate at the top of the valence bands while Ti 3d states dominate at the bottom of the conduction bands. When Fe is intercalated into TiO₂, the energy levels associated with Fe 3d electrons are lower than that of Ti 3d at the bottom of the conduction bands and these states do not qualitatively change the distribution of O 2p and Ti 3d states. Consequently, the bottom of the conduction bands has a decrease about 0.2 and 0.34 eV for the samples (Fe_{1/16}Ti_{15/16})O₂ and (Fe_{1/8}Ti_{7/8})O₂, respectively, and thus the electron transition energy from the valence band to the conduction band have a decrease about 0.2 and 0.34 eV, which induces a red shift of the optical absorption edge. The calculated results give a good explanation for experimental optical absorption broadening to longer wavelength in the Fe-TiO₂ nanorods [66].

5. Conclusions

Fe-TiO₂ nanorods with visible-light activity are easily prepared by an impregnating-calcination method using the titanate nanotube as precursor and Fe(NO₃)₃ as dopant. Fe-doping obviously influences the visible-light photocatalytic activity and microstructures of mesoporous TiO₂ nanorods. The photocatalytic activity of all Fe-TiO₂ nanorods is higher than that of Degussa P25 and pure TiO₂ nanorods. At $R_{Fe} = 0.5\%$, the photocatalytic activity of Fe-TiO₂ nanorods exceeds that of Degussa P25 by a factor of more than two times. This is due to the fact that an optimal Fe³⁺ concentration is beneficial to reduce the recombination of photo-generated electrons and holes, also the one-dimensional nanostructure can enhance the transfer and transport of charge carriers and the Fe-doping induces the shift of the absorption edge into the visible-light range with the narrowing of the band gap. The first-principle density functional theory (DFT) calculation further confirms the red shift of the absorption edges and the narrowing of the band gap of Fe-TiO₂ nanorods.

Acknowledgements

This work was partially supported by the National Natural Science Foundation of China (50625208, 20773097, 20877061). This work was also financially supported by the National Basic Research Program of China (2007CB613302 and 2009CB939704).

References

- [1] H. Tokudome, M. Miyauchi, Chem. Commun. (2004) 958.
- [2] X.M. Sun, Y.D. Li, Chem. Eur. J. 9 (2003) 2229.
- [3] J.G. Yu, J.C. Yu, W.K. Ho, L. Wu, X.C. Wang, J. Am. Chem. Soc. 126 (2004) 3422.
- [4] J.G. Yu, M.H. Zhou, Nanotechnology 19 (2008) 045606.
- [5] G.H. Du, Q. Chen, R.C. Che, Z.Y. Yuan, L.P. Peng, Appl. Phys. Lett. 79 (2001) 3702.
- [6] J.G. Yu, F.-R.F. Fan, S.L. Pan, V.M. Lynch, K.M. Omer, A.L. Bard, J. Am. Chem. Soc. 130 (2004) 7196.
- [7] H. Tokudome, M. Miyauchi, Angew. Chem. Int. Ed. 44 (2005) 1974.
- [8] M. Miyauchi, H. Tokudome, Thin Solid Films 515 (2006) 2091.
- [9] J.G. Yu, H.G. Yu, B. Cheng, X.J. Zhao, Q.J. Zhang, J. Photochem. Photobiol. A 182 (2006) 121.
- [10] Z.R.R. Tian, J.A. Voigt, J. Liu, B. McKenzie, H.F. Xu, J. Am. Chem. Soc. 125 (2003) 12384.
- [11] W.J. Dong, A. Cogbill, T.R. Zhang, S. Ghosh, Z.R. Tian, J. Phys. Chem. B 110 (2006) 16819.
- [12] H.G. Yu, J.G. Yu, B. Cheng, S.W. Liu, Nanotechnology 18 (2007) 065604.
- [13] T. Kasuga, M. Hiramatsu, A. Hoson, T. Sekino, K. Niihara, Langmuir 14 (1998) 3160.
- [14] T. Kasuga, M. Hiramatsu, A. Hoson, T. Sekino, K. Niihara, Adv. Mater. 11 (1999) 1307.
- [15] G.S. Kim, H.K. Seo, V.P. Godble, Y.S. Kim, O.B. Yang, H.S. Shin, Electrochem. Commun. 8 (2006) 961.
- [16] J.G. Yu, H.G. Yu, B. Cheng, C.C. Trapalis, J. Mol. Catal. A 249 (2006) 135.
- [17] H.G. Yu, J.G. Yu, B. Cheng, J. Mol. Catal. A 253 (2006) 99.
- [18] H.G. Yu, J.G. Yu, B. Cheng, M.H. Zhou, J. Solid State Chem. 179 (2006) 349.
- [19] H.G. Yu, J.G. Yu, B. Cheng, Chemosphere 66 (2007) 2050.
- [20] R.A. Doong, L.F. Chiang, Water Sci. Technol. 58 (2008) 1985.
- [21] P.H. Wen, H. Itoh, W.P. Tang, Q. Fang, Microporous Mesoporous Mater. 116 (2008) 147.
- [22] S. Ribbens, V. Meynen, G. Van Tendeloo, X. Ke, M. Mertens, B.U.W. Maes, P. Cool, E.F. Vansant, Microporous Mesoporous Mater. 114 (2008) 401.
- [23] M. Miyauchi, J. Mater. Chem. 18 (2008) 1858.
- [24] M. Ksibi, S. Rossignol, J.M. Tatibouet, C. Trapalis, Mater. Lett. 62 (2008) 4204.
- [25] J.A. Wang, R. Limas-Ballesteros, T. Lopez, et al. J. Phys. Chem. B 105 (40) (2001) 9692.
- [26] J.G. Yu, L.J. Zhang, B. Cheng, Y.R. Su, J. Phys. Chem. C 111 (2007) 10582.
- [27] M.R. Hoffmann, S.T. Martin, W. Choi, D.W. Bahnemann, Chem. Rev. 95 (1995) 69.
- [28] F.B. Li, X.Z. Li, Appl. Catal. A 228 (2002) 15.
- [29] S.P. Min, S.K. Kwon, B.I. Min, Phys. Rev. B 65 (2002) 161201.
- [30] J.G. Yu, H.G. Yu, H.T. Guo, M. Li, S. Mann, Small 4 (2008) 87.
- [31] Q.Y. Li, L.A. Chen, G.X. Lu, J. Phys. Chem. C 111 (2007) 11494.
- [32] C.Y. Wang, C. Bottcher, D.W. Bahnemann, J.K. Dohrmann, J. Mater. Chem. 13 (2003) 2322.
- [33] J.C. Yu, J.G. Yu, W.K. Ho, Z.T. Jiang, L.Z. Zhang, Chem. Mater. 14 (2002) 3808.
- [34] H. Yamashita, M. Harada, J. Misaka, M. Takeuchi, K. Ikeue, M. Anpo, J. Photochem. Photobiol. A 148 (2002) 257.
- [35] Z.H. Yuan, J.H. Jia, L.D. Zhang, Mater. Chem. Phys. 73 (2002) 323.
- [36] J.G. Yu, J.F. Xiong, B. Cheng, S.W. Liu, Appl. Catal. B 60 (2005) 211.
- [37] J.J. He, J.C. Zhao, T. Shen, H. Hidaka, N. Serpone, J. Phys. Chem. B 101 (1997) 9027.
- [38] J.G. Yu, J.F. Xiong, B. Cheng, Y. Yu, J.B. Wang, J. Solid State Chem. 178 (2005) 1968.
- [39] X.H. Tang, D.Y. Li, J. Phys. Chem. C 112 (2008) 5405.
- [40] W. Choi, A. Termin, M.R. Hoffmann, J. Phys. Chem. 98 (1994) 13669.
- [41] J.F. Zhu, F. Chen, J.L. Zhang, H.J. Chen, M. Anpo, J. Photochem. Photobiol. A 180 (2006) 196.
- [42] Y. Cong, J.L. Zhang, F. Chen, M. Anpo, D. He, J. Phys. Chem. C 111 (2007) 10618.
- [43] Q.H. Wei, W. Wen, Y. Ding, X.L. Zhen, M.M. Mathew, L. Laura, H. Jonathan, G. Oleg, J. Phys. Chem. C 111 (2007) 14339.
- [44] Y. Zhang, S.G. Ebbinghaus, A. Weidenkaff, T. Kurz, H.-A. Krug von Nidda, P.J. Klar, M. Gungerich, A. Reller, Chem. Mater. 15 (2003) 4028.
- [45] W. Huang, X. Tang, I. Felner, Y. Koltypin, A. Gedanken, Mater. Res. Bull. 37 (2002) 1721.
- [46] K.S.W. Sing, D.H. Everett, R.A.W. Haul, L. Moscou, R.A. Pierotti, J. Rouquerol, T. Siemieniowska, Pure Appl. Chem. 57 (1985) 603.
- [47] S.J. Gregg, K.S.W. Sing, Adsorption, Surface Area and Porosity, Academic Press, London, 1982.
- [48] J.G. Yu, J.C. Yu, M.K.P. Leung, W.K. Ho, B. Cheng, X.J. Zhao, J.C. Zhao, J. Catal. 217 (2003) 69.
- [49] K. Ishibashi, A. Fujishima, T. Watanabe, K. Hashimoto, Electrochem. Commun. 2 (2000) 207.
- [50] Q. Xiao, Z.C. Si, J. Zhang, C. Xiao, X.K. Tan, J. Hazard. Mater. 150 (2008) 62.
- [51] J.G. Yu, G.H. Wang, B. Cheng, M.H. Zhou, Appl. Catal. B 69 (2007) 171.
- [52] J.G. Yu, Y.R. Su, B. Cheng, Adv. Funct. Mater. 17 (2007) 1984.
- [53] J.P. Perdew, J.A. Chevary, S.H. Vosko, K.A. Jackson, M.R. Pederson, D.J. Singh, C. Fiolhais, Phys. Rev. B 46 (1992) 6671.
- [54] H.J. Monkhorst, J.D. Pack, Phys. Rev. B 13 (1976) 5188.
- [55] M.H. Zhou, J.G. Yu, B. Cheng, J. Hazard. Mater. 137 (2006) 1838.
- [56] M.H. Zhou, J.G. Yu, B. Cheng, H.G. Yu, Mater. Chem. Phys. 93 (2005) 159.
- [57] J.G. Yu, H.G. Yu, C.H. Ao, S.C. Lee, J.C. Yu, W.K. Ho, Thin Solid Films 496 (2006) 273.
- [58] J.F. Moulder, W.F. Stickle, P.E. Sobol, K.D. Bomben, Handbook of X-ray Photoelectron Spectroscopy, Physical Electronics Division, Perkin-Elmer Corporation, Eden Prairie, MN, USA, 1992.
- [59] Z. Ambrus, N. Balazs, T. Alapi, G. Wittmann, P. Sipos, A. Dombi, K. Mogyorosi, Appl. Catal. B 81 (2008) 27.
- [60] J. Zhu, W. Zheng, B. He, J. Zhang, M. Anpo, J. Mol. Catal. A 216 (2004) 35.
- [61] J.G. Yu, X.X. Yu, Environ. Sci. Technol. 42 (2008) 4902.
- [62] E.M. Patterson, C.E. Shelden, B.H. Stockton, Appl. Opt. 16 (1977) 729.
- [63] N. Serpone, D. Lawless, R. Khairutdinov, J. Phys. Chem. 99 (1995) 16646.
- [64] Z. Zhang, C.C. Wang, R. Zakaria, J.Y. Ying, J. Phys. Chem. B 102 (1998) 10871.
- [65] C. DiValentin, G. Pacchioni, A. Selloni, Phys. Rev. B 70 (2004) 085116.
- [66] K. Yang, Y. Dai, B. Huang, J. Phys. Chem. C 111 (2007) 18985.